Relationships between arc plasma jet properties and plasma/liquid interaction mechanisms for the deposition of nanostructured ceramic coatings

Vincent Rat, Marguerite Bienia, Gayatri Dasharath D Dhamale, Fabrice Mavier, Céline Ruelle, Simon Goutier

▶ **To cite this version:**

Vincent Rat, Marguerite Bienia, Gayatri Dasharath D Dhamale, Fabrice Mavier, Céline Ruelle, et al.. Relationships between arc plasma jet properties and plasma/liquid interaction mechanisms for the deposition of nanostructured ceramic coatings. Plasma Physics and Controlled Fusion, In press, ⟨10.1088/1361-6587/ac3c39⟩. ⟨hal-03453757⟩

HAL Id: hal-03453757

https://hal.science/hal-03453757v1

Submitted on 28 Nov 2021

Relationships between arc plasma jet properties and plasma/liquid interaction mechanisms for the deposition of nanostructured ceramic coatings

V. Rat[1], M. Bienia[1], G.D. Dhamale[2], F. Mavier[1], C. Ruelle[1], S. Goutier[1]

[1] Institute of Research for Ceramics IRCER UMR7315, CNRS, University de Limoges, France

[2] Institute for Plasma Research, Gujarat, India

Abstract

Ceramic nanostructured coatings with intermediate thicknesses between 10 and 100 µm exhibit improved thermal and mechanical properties for thermal barrier coatings or wear resistant coatings. Such coatings comply with the technical requirements of aeronautical and automotive applications. This implies to develop deposition processes with high throughput and deposition rates promoting the formation of nanostructured coatings. The use of a liquid phase as a carrier medium of nanoparticles or of solution precursors has been shown to be of major interest when being injected within a thermal plasma jet. The as-sprayed materials can form ceramic nanostructured coatings provided the liquid injection encompassing the physicochemical properties of liquid and its injection method copes with the plasma properties. Especially the repeatability of the interaction phenomena between the liquid phase and the arc jet has a key role in the efficiency deposition so that some research efforts are devoted to stabilize the arc while a liquid jet is continuously injected within the plasma. Alternatively a pulsed arc plasma jet can be generated and associated with a time-phased injection of droplets. This paper presents the different issues related to the arc plasma properties produced by direct plasma torches including the arc instabilities and their influence on plasma/liquid interaction mechanisms leading to the formation of nanomaterials. A focus is made on pulsed plasma spraying associated with a synchronized injection of microsized droplets by means of an inkjet printing method.

Key words: thermal plasma, plasma torches, arc instabilities, liquid injection, ceramic coatings growth

1. Introduction

The development of plasma spraying of liquid feedstocks has started at the end of the 90’s with the first papers describing the formation of nanostructured coatings or the synthesis of nanosized particles in thermal plasma jets (1–3). The improvement of properties of plasma sprayed coatings imparting new features at nanoscale underlay the motivations of such an original research. Thereafter, two main trends have emerged depending on the nature of liquid feedstocks injected in the plasma. On the one hand, Suspension Plasma Spraying (SPS) consists in forming a suspension of submicron particles dispersed within a solvent. On the other hand, Solution Precursor Plasma Spraying (SPPS) offers the possibility to inject a precursor solution which the metallic element aimed at being sprayed is dissolved as a salt in a solvent. These deposition methods have turned out to be flexible enough to consider the association of the different elements of a solid oxide fuel cell in a single step process with the control of the chemical composition and the coating architecture (4,5). The use of SPS and SPPS for manufacturing Thermal Barrier Coatings have been also extensively studied and reviewed especially for the columnar microstructures of coatings, the control of the porosity content and size, and segmentation cracks (6–10). Moreover, the typical coating thicknesses can be varied between a few tens and a few hundreds of micrometers bridging the gap between the thin films and the coatings constructed by conventional plasma spraying.

The understanding and the control of coating properties are obviously deeply related to the complex and intricate phenomena governing the liquid precursor treatment by the plasma jet from the early stages of the liquid injection to the impact of sprayed materials onto the substrate. They encompass the injection of liquid as a droplets or liquid jet, the liquid fragmentation and its evaporation, the solid particles formation (or in-fight agglomeration) competing with their possible evaporation during their transport in the plasma jet until the coating growth which can be affected by gas phase combustion reactions resulting from the solvent nature especially in the case of SPPS (4,10,11). Even though the liquid has a basic function of a carrying medium for particles in SPS giving them enough momentum to penetrate the plasma jet, the liquid properties not only affect profoundly the entire history of solid materials in their interaction with the plasma but also the coating growth. Consequently, one of the major challenges is to control the plasma properties (enthalpy, speed, flow regime of the plasma jet) and therefore the dynamics of the arc which in turn strongly interacts with the plasma torch design.

This paper gives an overview of the main challenges and current issues encountered in plasma spraying of liquid feedstocks by focusing on the inter-dependent key parts in the deposition process. Section 1 presents the typical arc plasma torches currently used in SPS and SPPS. Classification of torches is made according to their specific enthalpy but also to their stability. The properties of the liquid injected as ceramic ink in the plasma are described and the in-flight phenomena are described in section 2. Before concluding, the last section presents the typical features of as-sprayed coatings and discuss the key parameters to form nanostructures.

2. Current non-transferred plasma torches

2.1 Energetic features

A plasma torch is a conversion tool that permits to change the electrical energy into thermal energy in order to melt and spray materials. The efficiency of this conversion is deeply dependent upon the torch design (geometry of the electrodes, relative position of cathode/anode) and the experimental parameters such as the arc current, the chemical composition of the gas flow rates and their mass flow rates. As depicted in Figure 1, the Conventional non-transferred Torch (CT) are equipped with a thoriated (or lanthanum doped) rod-cathode and a water-cooled anode nozzle that form an inter-electrode space where the arc is confined and burns. The electrical power P_e is measured as $P_e = \bar{V} I$ where $\bar{V}$ and I are respectively the mean arc voltage and the arc current.

The specific enthalpy available to treat materials results from an energy balance that obeys to the following equation at steady state:

$$\rho u \frac{\partial h}{\partial z} = \sigma E^2 - \boldsymbol{\nabla}.\boldsymbol{q} - q_r \qquad (1)$$

where ρ, u and h are respectively the plasma density, the axial plasma speed and the specific enthalpy.

The first term on the right-hand side is the Joule heating where σ and E are respectively the electrical conductivity and the electric field. The second and third terms on the right-hand side are the power densities lost by the arc respectively due to the thermal conduction where **q** is the heat flux, and due to radiation.

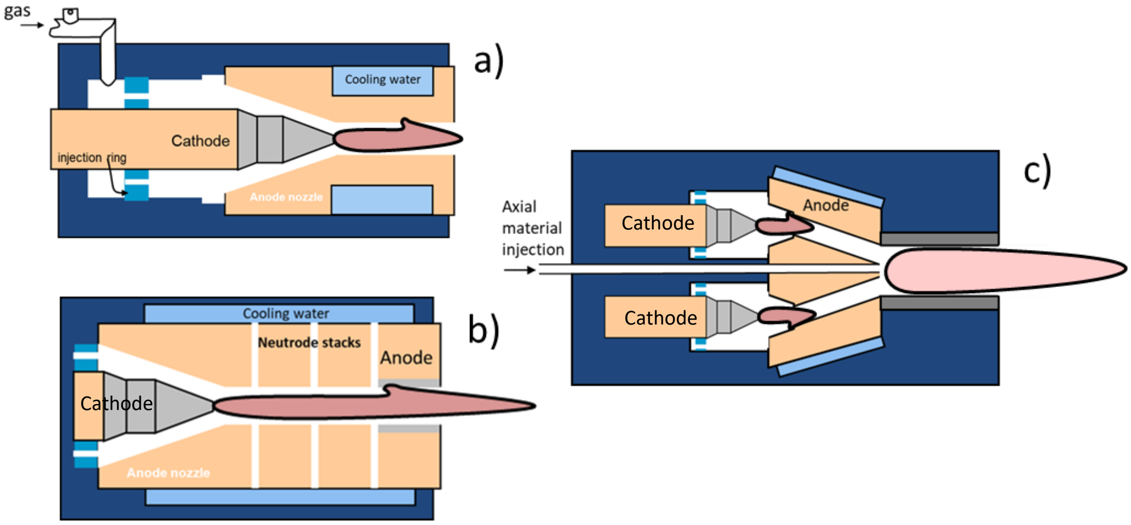

Figure 1: Current non-transferred plasma torches used for liquid feedstock spraying

a) Conventional torch CT, b) Segmented plasma Torch ST, c) Axial Multi-electrode Torch AMT

The power absorbed by the electrodes walls can be determined by performing a calorimetric measurement on the water-cooling system. It basically consists in measuring the temperature difference ΔT between the output and input water on the cooling line of the torch body. The heat losses are given by $Q_{loss} = \dot{m}_w C_P \Delta T$ where $\dot{m}_w$ and C_P are respectively the water mass flow rate and the water specific heat. The measured heat losses are spread all over the inner electrodes walls and encompass the contributions of convective, radiative and electrical processes so that the overall heat flux ranges between 10^6 to 10^8 W.m^{-2}. Actually, the heat losses due the arc attachment only, i.e. corresponding to the heat flux of electrical origin, can reach 10^9-10^{10} W.m^{-2} due to highly localized arc root. This intensified heat flux at the arc root is responsible for the anode erosion whose the characteristic time τ_m of melting can be evaluated under the simplified assumption of a semi-infinite anode wall exposed to a heat flux φ_{elec}, i.e. $\tau_m = \pi\big(\kappa_a(T_m - T_w)\big)^2/\alpha(2\varphi_{elec})^2$ where κ_a, α, T_m are respectively the thermal conductivity, the thermal diffusivity and the melting temperature of the anode, and T_w is the temperature of the anode wall (12). In the case of a typical copper anode, the time τ_m is roughly 50 µs for a heat flux of 5x10^9 W.m^{-2}. It means that the arc root cannot be fixed longer than τ_m otherwise a rapid destruction of the anode wall can be expected. Consequently, despite the harmful influence of the arc instabilities on the plasma jet at nozzle exit, they do allow the anode wall to sustain the heat load caused by the arc attachment. The thermal efficiency of the plasma torch, i.e. its capability in converting the electrical energy into thermal energy, is given by $\eta = 1 - Q_{loss}/P_e$. The mean specific enthalpy produced by the torch and available at nozzle exit is basically evaluated by $\bar{h}_0 = \eta \bar{V} I/\dot{m}$ where $\dot{m}$ is the mass flow rate of plasma forming gases. It is worth noting that it also includes the specific kinetic energy of the plasma jet so that $\bar{h}_0 = \bar{h}_L + \bar{u}^2/2$ where $\bar{h}_L$ is the mean specific enthalpy at nozzle exit. By considering that $\bar{u}$ is close to 1000 m.s^{-1} at atmospheric pressure, the kinetic energy only represents less than 10% of the total energy and is usually neglected.

The measured enthalpy at nozzle exit is a quantity averaged in time but also in the cross section at nozzle exit, i.e. $\bar{h}_0 = \frac{8}{d^2}\int_0^{\frac{d}{2}} \bar{h}(r) r dr$ where $\bar{h}(r)$ is the time-averaged radial enthalpy profile and d the inner nozzle diameter. The enthalpy is linked to temperature thanks to thermodynamic data that permits to evaluate the mean plasma temperature at nozzle exit under the LTE assumption.

By considering that the plasma speed increases from the anode wall to the center of the arc whereas the plasma density has a reverse dependence, the density of mass flux is roughly constant so that $\rho\bar{u} = 4\dot{m}/\pi d^2$ where $\bar{u}$ is the mean plasma speed at nozzle exit. This simplified relationship highlights the dependence of the speed on the mass flow rate of plasma forming and the mean temperature through the plasma density. This intricate dependence is also reported in the correlation equation given by Planche *et al.* (13) where the centerline speed v_{max} of speed profile is written as $v_{max} = K\dot{m}^{0.21} I^{0.44}/d^{1.96}$ where K is correlation constant depending on plasma forming gases composition. Another approach gives $\bar{u} = \bar{h}_0 \dot{m}(\gamma - 1)/P_a S \gamma$ where γ, S and P_a are the isentropic exponent, the nozzle cross section, the pressure at nozzle exit, and establishes a straightforward dependence on the mean specific enthalpy (14). Consequently, mean thermal energy and plasma momentum can be in principle described by measuring of the specific enthalpy which can be used as a criterion of torch classification.

Different DC plasma torches families are currently used in plasma spraying of liquid feedstocks, namely the CT torches, but also the Segmented Torches (ST, sometimes named cascade torch) and the Axial Multi-electrode Torches (AMT). In the ST torches (Figure 1b), a stack of copper rings electrically insulated from each other, called neutrodes or inter-electrode insert, permits to increase the arc length, and hence the arc voltage and electrical power, but also improves the arc stability. The thickness of a copper ring must satisfy the condition $\int_0^e E dz < V_a + V_c$ where E, z, V_a and V_c are respectively the electric field of the arc column, the axial coordinate, the anode and cathode drop voltages, meaning that the arc cannot exist if the column drop voltage is lower than the electrode drop voltages, which can be estimated between 10 and 20 V for typical plasma forming gases in plasma spraying. Zhukov and Zasypkin have reviewed the so-called linear plasma torches dating back to the 80's and permitting to promote a fixed arc length either by means of a ledge in the anode wall or by the use of an inter-electrode insert (15). Several commercial versions for research and industrial purposes are used today (16–19). The addition of cathodes properly arranged is aimed at mitigating the impact of electrode erosion by reducing the arc current of each cathode while maintaining high electrical power. This torch belongs to the Multi-electrode Torch (MT) family. The axial injection of materials usually permits better material processing which implies the injection in the region of merging plasma jet generated by several CT torches combined within a unique torch body. This torch family refers to Axial Multi-electrode Torch (AMT) in Figure 1c. Note that Figure 1c only depicts two cathodes for legibility reason but three arc plasma jets usually merge together to form the main high-temperature flow where materials are plasma sprayed. Note that Figure 2a shows the current/voltage characteristics of the above-mentioned current plasma torches families and their corresponding mean specific enthalpy $\bar{h}_0$ dependence on the electrical power in Figure 2b. The purpose of Figure 2b is to point out the particular features of different plasma torches families from some reported results. It must be underlined that scarce studies presents complete set of measurements of plasma torches used in plasma spraying, especially for ST and AMT torches. The labels CT, ST, MT and AMT respectively refers to the torches F4, SinplexPro, TriplexPro-210 (Oerlikon Metco) and Axial III (Mettech) in experiments. Different plasma forming gases, mixtures and flow rates (Ar, H_2, N_2, He) are used. For ST torch, three arc voltages are obtained for the same current because of changes in mass flow rates in Ar-H_2 mixtures which affect the enthalpy through the arc voltage and the total gas mass flow rate. For the AMT, the specific enthalpy was evaluated assuming a thermal efficiency of 60% (20).

The torches CT, ST and MT operate with arc current ranging between 50 and 600 A while the arc voltage usually does not exceed 350 V for typical argon, hydrogen, nitrogen and helium gas mixtures. The arc length fixation for ST and MT torches results in higher voltage and electrical power than for CT torches. The CT torches have a well-known decreasing feature of voltage as function of current for given plasma forming gases flow rate. In this case, two coincident effects are combined to lower the arc voltage despite the increase of the current. On the one hand, the electrical conduction of the arc is improved as the arc current is increased due to an increased arc diameter. On the other hand, the arc length is also reduced because the arc can reattach closer to the cathode at higher arc current. It can be mentioned that, at very high current, the electrical field of the arc column can increase to sustain the electrical discharge to give rise to an increasing feature of the arc voltage (15). The ST torches have instead an increasing feature as shown in Figure 2a resulting mainly from the arc length more or less constant and a dominant effect of the increase current on the electric arc conduction. It means that the amplitude of arc voltage fluctuations compared to the mean voltage is weak, usually less than 10%. It is interesting to note that the AMT torch can operated at very high electrical power. Actually, it combines three torches, each working at 230 A (20) . The CT, ST, MT and AMT torches can reach moderate specific enthalpy below 40 MJ.kg^{-1} due to moderate electrical power but also high mass flow of plasma forming gases that require energy to be ionized. It is must be underlined that the torch classification proposed in Figure 2 does not allow inferring the properties profiles of the plasma jet at nozzle exit. For example, Planche *et al.* shows that the centerline speed v_{max} increases as $\dot{m}$ increases but the speed profiles also become narrower (13). Moreover, it turns out the above plasma torches currently used in plasma spraying applications generate turbulent plasma jet downstream the nozzle exit leading strong air cooling and strong decrease of plasma temperature and velocity (21).

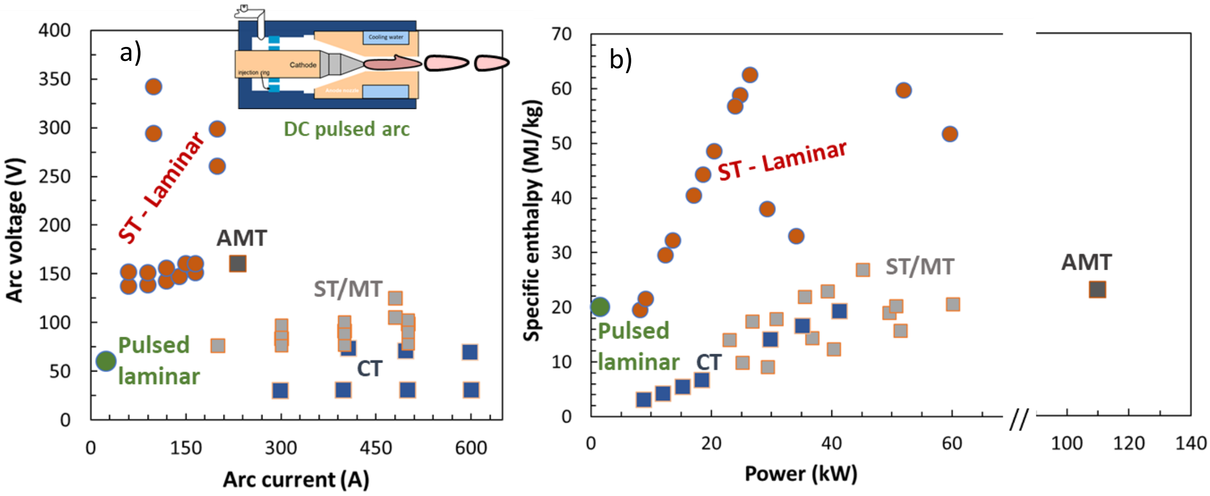

Figure 2: a) Current/voltage characteristics of main DC plasma torches families used in plasma spraying of liquid feedstocks, Conventional Torch (CT), Segmented Torch (ST), Multi-electrode Torch (MT), Axial Multi-electrode Torch (AMT). b) Specific enthalpy dependence on electrical power (20,22–24).

The turbulence is described from the formation of ring vortices around the jet close to the nozzle exit bringing about the surrounding air engulfment (21). However, in the case of highly fluctuating torch (CT), the turbulence of the plasma jet originates mainly from the arc motion inside the torch (25). Consequently, an increasing number of studies are also devoted to the development of ST torches operating in laminar mode with lower arc current and much higher arc voltage, up to 350 V (26–29). Solonenko et al. interestingly discuss the advantages of plasma torches working at low Reynolds number (26). They operate at low gas mass flow rate (<1 g/s) and low arc current (<200 A). The adjustment of the length to diameter ratio of the arc channel permits to reach high voltage by elongation and constriction of the arc. It results that laminar torches attain quite high arc voltage and also high specific enthalpy as shown in Figure 2. Temperature and velocity fields are also higher than in the case of CT torches (29) meaning that the decrease of mass flow rate in comparison with torches generating turbulent plasma jet is compensated by higher specific enthalpy. The association of neutrodes in the inter-electrode insert and an optimized nozzle with a backward-facing step allows reaching laminar plasma jets as long as 500 mm from the nozzle along with a very large extension of high specific enthalpy in the plasma jet. Depending on the aperture size and length of the step in the nozzle wall, the gas from the surroundings flows into the nozzle and interacts with the internal closed vortex created by the detachment of the dynamic boundary layer due to the stepped nozzle. It results in the suppression of the closed vortex and stabilizes the outflowing jet (26). It is also been shown that a trumpet-like shape of the anode favors the expansion of arc column and reduces the compression effect of the cold boundary around the arc (29).

A low powered DC torch has been developed to operate in a self-sustained pulsed mode producing a pulsed laminar plasma jet depicted in Figure 2a. The purpose was to improve the plasma heat and momentum transfers to droplets by the assistance of a phased liquid injection (30). This torch operates at very low current (<25 A) and provides specific enthalpy as high as that of CT torch (~20 MJ.kg^{-1}) because of low mass flow rate of nitrogen plasma forming gas (< 3 slm). It results that the plasma speed is more than one order of magnitude smaller than that of CT torches, i.e. close to 70 m.s^{-1} (31).

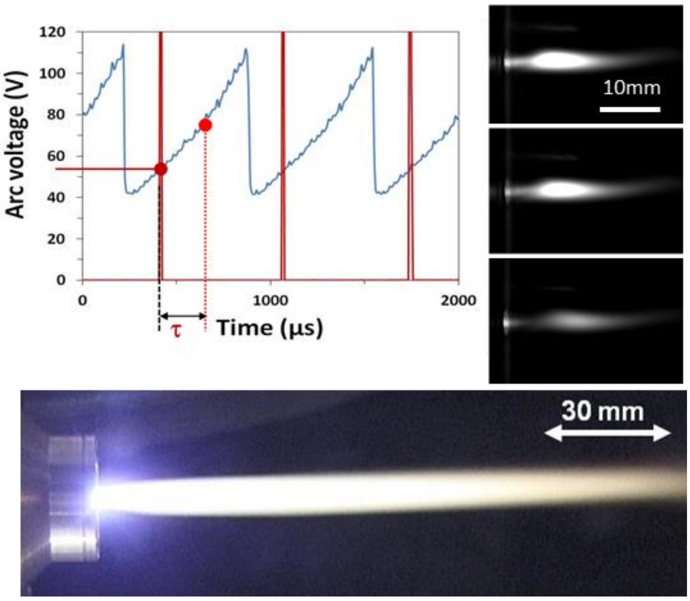

Figure 3. Arc voltage signal of dc pulsed torch and imaging of pseudo laminar jet (30)

2.2 Arc control for liquid injection: pulsed DC torch

The control of the arc motion in DC torch has been the subject of many studies over several decades. It becomes a more challenging task especially today for elaborating coatings with the desired multiple functionalities evidently linked to their complex chemical composition, their nano/microstructure including (nano)porosities, cracks and also their crystallographic structure. Consequently, the current DC torches (ST, MT, AMT configurations) are innovative plasma systems where not only the variations in plasma properties downstream the nozzle exit are intended to be reduced, either by limiting the arc motion or by merging several arcjets, but also where the problem of the electrode erosion is considered by reducing the arc current or by using appropriate plasma forming gases. The latter affect the arc attachment constriction and therefore the current density through the Cold Boundary Layer (CBL) between the arc column and the anode wall (32,33). The anode attachment modes (diffuse or constricted) are expected to strongly affect the erosion. They are dependent on arc current and gases but also on the anode design, operating pressure and applied magnetic field (34–36).

Thus, a stabilized plasma implies a stable and continuous injection of liquid feedstock leading to reproducible plasma/liquid interactions. However, if the arc motion is a major source of instabilities, others sources may originate in the interaction with the column liquid of droplets due to particularly the injection mode (axial or radial), the liquid injection technology or the injection location as shown in the next section. Consequently, a dc pulsed torch was designed to cope with these requirements and was associated with a phased radial liquid injection driven by a piezoelectric dispenser and a time delay generator (37). While the arc motion in a DC torch is ruled by the unbalance between the Lorenz and hydrodynamic forces, the arc reattaches through the CBL when the arc voltage $V_{arc}(z,t)$ reaches a critical arc voltage $V_b = e_z E_b$ depending on both the mean breakdown electric field E_b (a few tens of kV.m^{-1}) and the thickness of the CBL e_z (30,38). Shao et al. have recently highlighted in details the dynamics of the restrike mode along with time-resolved temperature measurements (39).

They obtained typical saw-tooth shape signals (restrike signal) for the arc voltage V_{arc} for which the frequency f_r and the amplitude δ_v are linked together by $f_r = (dV_{arc}/dt)/\delta_v$ and are deeply linked to the arc current, plasma gases and more generally to the specific enthalpy as explained in the previous section. Indeed, the rate of increase of the arc voltage is related to the mean plasma speed by $dV_{arc}/dt \sim E_c \bar{u}$ where E_c is the mean electric field of the arc column.

Figure 3 displays a typical restrike signal fluctuating at 1.4 kHz with large amplitudes (30). A pseudo-laminar pure nitrogen plasma jet is obtained as shown with imaging performed at low frame rate but actually the arcjet is composed of high enthalpy regions which are released by the torch at 1.4 kHz frequency. Furthermore, it is expected that f_r can be tuned by modifying the thickness of CBL e_z. The current conservation equation permits to anticipate that an arc current modulation affects the arc radius $r_{arc} = d/2 - e_z$ but also the electric field according to the electrical current conservation equation $I = 2\pi E(z,t) \int_0^{r_{arc}} \sigma(r,z,t) r dr$. A time-modulation of the arc current following $I(t) = I_0\left(1 + \alpha sin(2\pi f_0 t)\right)$ has also been shown to stabilize the DC torch in a forced pulsed mode, i.e. for $f_0 = f_r$, where α and f_0 are the imposed current amplitude and frequency respectively. Figure 4 displays the observation of the arc attachments at nozzle exit at different moments in the arc voltage and applied current. The study highlights different voltage patterns with single or double restrikes as shown in Figure 4.

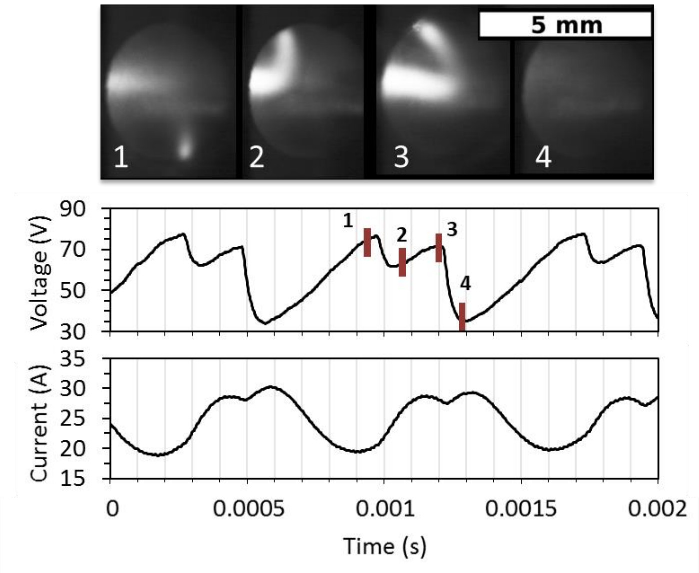

Figure 4. Time-resolved imaging of the attachment close to the nozzle exit of an arc under modulated current (31).

Between pictures 1 and 2, the arc has undergone a small amplitude voltage restrike jump to the opposite side while the arc current has low value just before restrike (#1). Between pictures 3 and 4 a large amplitude voltage jump is observed whereas the arc current is high just before restrike (#3). At last, in pictures 1 and 3, the arc is attached at nozzle exit with almost the same length but it is clearly observed a smaller arc attachment radius in case of picture 1. Consequently, the current modulation tends to favor the arc reattachment on the one hand at high current due to high arc radius (low CBL thickness) and on the other hand at low current probably due to an electric field intensification to maintain the electrical discharge (31). It is worth underlining that the above interpretation is based on the existence of a single arc attachment observed close to the nozzle exit and should be backed by end-on arc images of the arc inside the torch to discard the assumption of possible multiple arc roots as shown by Dorier *et al* (33), Ghorui *et al* (40), and Qiang *et al* (41).

The association of time-resolved temperature measurements and a simplified model of heat transfer in the torch gives the dynamics of the specific enthalpy at nozzle exit, i.e. its amplitude modulation considering the thermal efficiency of the torch η and also the time-shift between voltage and enthalpy which actually corresponds to the residence of plasma in the arc channel (proportional to $\bar{u}$), i.e. the duration needed by the torch to release the net thermal energy stored inside the arc channel between two consecutive restrike jumps.

The classification of torches according to the enthalpy is essential because it determines the thermal energy available and indirectly the plasma speed for momentum transfer. However, it is worth underlining that it does not account for the load effect due to the injection, i.e. the two-way heat and momentum transfers that alters the plasma temperature and velocity fields. The typical mass flow rates of liquids injected in plasma generated by CT torches (~35-40kW) are close to 20-30 g.min^{-1}. They roughly linearly increase as the electrical power increases to reach about 90 g.min^{-1} for AMT torches. As insightfully discussed by Jordan *et al.* (10), only 10% of the net torch power is transferred to the liquid and more than half of the energy is consumed by the evaporation of the liquid phase. As a result, plasma spraying of liquid feedstock requires substantial energy to evaporate the liquid so that the material flow rate contained in the liquid phase and used to form the coatings is lower than when spraying solid material alone (typically 4 times lower) (10). It results that the deposition rate of solid materials to form coatings is actually strongly limited by the liquid phase.

Consequently, attention must be paid to the decomposition mechanisms of the injected liquid, including liquid fragmentation, evaporation, in-flight solid material formation and transport.

3. Plasma liquid treatment

This section first focuses on the ceramic ink requirements used in piezoelectric printed head for liquid injection. Second, plasma-liquid interaction phenomena are briefly presented highlighting the differences when operating with CT or dc pulsed torch.

3.1 Ink formulation

A ceramic ink is a suspension of solid particles which the properties were made compatible with the piezoelectric injection of the printing device. Indeed, the ink formulation must meet several requirements in order to be ejected properly as calibrated droplets. First, the ejection ratio Z has to be considered as follows:

$$Z = \frac{\sqrt{R\rho\sigma}}{\eta} = \frac{1}{Oh} = \frac{Re}{\sqrt{We}} \tag{2}$$

with R, ρ, σ and η respectively the nozzle radius, ink density, surface tension and viscosity. This number accounts for the relative contribution of inertial, viscous and interfacial forces. It permits to establish a criterion of formation of a reproducible single droplet and must fall into the range $1 < Z < 10$. If Z is too low, the liquid filament ejected does not break due to viscous damping of instabilities. If it is too high, the breakup generates a spray of multiple satellite droplets (42). The typical breakup time is of the order of the µs, and the generated drops has a velocity of a few m.s^{-1} (43). Moreover, depending on the printhead used, viscosity and surface tension may also have an operational range. For the former, the typical shear stress in the nozzle is of the order of 10^5 s^{-1}, so an ink too viscous cannot be pushed through. For the latter, pooling on the printhead must be avoided, and this parameter is less critical for the case of capillary nozzles. These properties can easily be tuned by adding viscous solvents and surfactant molecules. In the case of SPPS, Mavier *et al.* dissolved an aluminum nitrate nonahydrate ($Al(NO_3)_3.9H_2O$) salt into deionized water with glycerol and BRIJ surfactant to respectively adjust the viscosity and surface tension. Ammonia was also used to increase the solution pH which affects the limit of solubility (37). In the case of SPS with particulate inks, additional properties need to be taken into account, namely 90% of the particle size distribution must be smaller than $R/50$ to prevent from clogging where R is the diameter of the printhead. Since $R \approx 50$ µm, the typical maximum particle size must fall below 1 µm.

Moreover, to avoid the formation of large agglomerates and prevent sedimentation in the printhead reservoir, the suspension must be stable in time, i.e. the inter-particle interactions must be controlled. They are often described by the Derjaguin-Landau-Vervey-Overbeek (DLVO) potential involving the van der Waals attraction (vdW) and the electrostatic interactions (ES), which can be attractive or repulsive, $V(r) = V_{ES}(r) + V_{vdW}(r)$ r where r the distance between the particles (44). The mathematical description for the interaction potential is sometimes found in the literature as the sum of Lennard-Jones potential and Yukawa potential for electrostatic repulsion (45). These embed all contributions, including depletion attraction and hard-core repulsion. The resulting potential may have different profiles:

1. No electrostatic interactions: strongly attractive with a minimum at $r = r_0$ where r_0 is the particle diameter. Hard core repulsion may be present to avoid overlapping.

2. Mild electrostatic interactions resulting in a potential barrier lower than $10k_BT$ and a shallow secondary minimum: weak aggregation, reversible, where k_B and T are respectively the Boltzmann constant and the temperature of the suspension.
3. Strong electrostatic repulsion resulting in a potential barrier larger than $10k_BT$: the suspension is considered stable.

When oxides are dispersed in an aqueous medium, an electrical double layer is formed around the particle due to hydration reactions on the particle. Depending on the nature of the oxide and the pH value, OH^- or H^+ ions are formed on the surface. Here are the reactions for titanium dioxide in water used for SPS (37):

$$\begin{cases} 2H_2O \rightleftharpoons H_3O^+ + OH^- \\ TiOH + H_3O^+ \rightleftharpoons TiOH_2^+ + H_2O \\ TiOH + OH^- \rightleftharpoons TiO^- + H_2O \end{cases}$$

A net charge thus appears on the particle, and the counter-ions are distributed around it within a typical distance called the Debye length κ^{-1}:

$$\kappa^{-1} = \sqrt{k_BT\frac{\varepsilon_0\varepsilon_r}{2e^2IN_A}} \qquad (3)$$

with $\varepsilon_0\varepsilon_r$ the dielectric permittivity of the medium, e the elementary charge, N_A the Avogadro number and I the ionic strength $I = \frac{1}{2}\sum c_i\, z_i^2$.(c_i being the molar concentration of the species in the solution and z_i its charge number).

For example, Al_2O_3 is positively charged for pH<9 and negatively for pH>9. This zero-charge value is 5.5 for TiO_2 and 2 for SiO_2.

The larger the surface charge and the Debye length, the more electrostatic stabilization occurs in the suspension. Surface charge can be tuned by varying the pH of the suspension. The Debye length depends on the concentration of the ionized species in the medium.

When the surface charge generation and electrostatic repulsion are not enough to counteract the van der Waals attraction, dispersing additives are used. They can have different actions:

- Steric repulsion: large polymers adsorbed on the particles ensure that the particles do not enter within a close range to each other. For non-polar solvents, only steric dispersants can be used.
- Electrostatic repulsion: ionized salts adsorb on the surfaces of the particles, leading to an increase of surface charge (for example: dibasic ammonium citrate (DBAC))

- Electro-steric repulsion: both effects may be combined for the case of large polymeric electrolytes which develop both surface charge and steric repulsion (for example: Darvan C)

The amount of dispersant needs to be perfectly adjusted because lack or excess both lead to attraction, due to depletion forces. The specific surface area of the particles is a physical quantity to be considered to do so.

3.2 Plasma liquid interactions

Liquids are usually injected in the plasma jet as a liquid column by means of a mechanical injection or as droplets from an atomization spray. The comparison of the characteristic times of fragmentation and evaporation shows differences by several orders of magnitude in favour of fragmentation (tens of µs) which was experimentally and numerically shown (11,41).

As shown in Figure 5A, the liquid column (~150µm in diameter) is primarily fragmented into large liquids ligaments and drops, and a secondary fragmentation results in droplets size distribution of a few tens of micrometres depending on many parameters like the liquid flow rate, the injector position with respect to the nozzle and its injection angle.

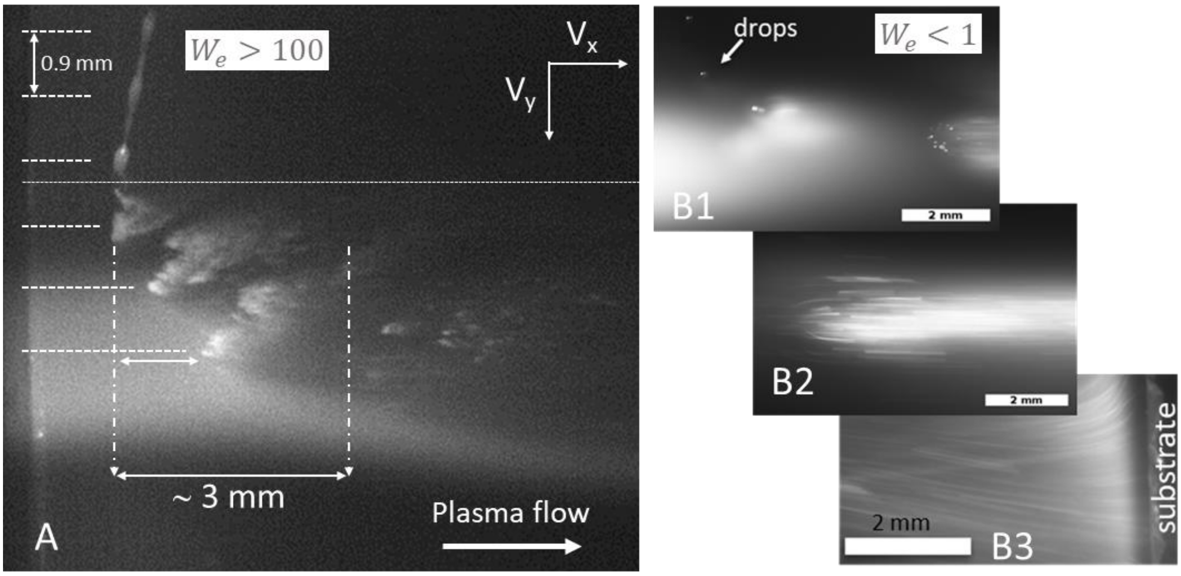

Figure 5. Time-resolved imaging of liquid injection in a dc arc plasma jet at nozzle exit (CT torch): A) Mechanical liquid column injection of a suspension of Yttria Stabilized Zirconia submicron particles, 10µs exposure time, 26.6 m.s^{-1} injection speed, Ar-H_2 plasma (45-15 slm), 500 A. B) Piezoelectric droplet injection of aluminum nitrate precursor solution, 50µs exposure time, 3.2 m.s^{-1} injection speed, N2 plasma (2 slm), 25 A (dc pulsed arc). B1: early stages of thermal fragmentation, B2: transport of materials, B3: plasma jet streamlines close to the substrate. W_e is the Weber number.

Jaddidi *et al.* (46,47) have exhaustively reviewed heat transfers in SPS process but they have also highlighted the classification of breakup phenomena of liquid columns for the primary fragmentation and of drops for the secondary one according to the plasma gas Weber number ($W_e = \rho_G U_G^2 D/\sigma$), the momentum flux ratio $q = \rho_L U_L^2/\rho_G U_G^2$, and the Ohnesorge number of drops $Oh = \mu_L/\sqrt{\rho_L d_L \sigma_L}$ where $(\rho, U)_G$ and $(\rho, U)_L$ are respectively the (density, relative velocity) of the plasma gas and the liquid phase, σ_L is the surface tension, μ_L the dynamic viscosity of the liquid phase, D is the diameter of liquid column and d_L the diameter of the drop. According to the considerations of the previous section related to the specific enthalpy and plasma speed, a mechanical fragmentation is expected due to $W_e > 100$ while the liquid column momentum flux, or its dynamic pressure, remains higher that of the plasma jet (q > 1). It results that the liquid penetration in the core of the plasma has to be adjusted following the plasma properties to fulfill q > 1. Due to the plasma cross-flow shearing the surface of the liquid column, surface waves grow, even outside the plasma as shown in Figure 5A, to produce ligaments or threads lengthening in the plasma flow direction and breaking up into liquid fragments. It is worth underlining that the dynamic pressure of the plasma is strongly non-uniform in the radial direction because of the temperature dependence of plasma density. As pointed out by Meillot *et al.* (48), the Weber number may be high in the fringes of the plasma due to high velocity gradient and high plasma density.

When travelling the hot plasma core, ligaments and drops undergo catastrophic fragmentation at high Weber numbers ($W_e > 100$) resulting into droplets (~ tens of µm in diameter) due to Kelvin-Helmholtz and Rayleigh-Taylor fluid instabilities (46,49,50). Figure 5A displays that the liquid column, injected with a speed of about 30 m.s^{-1}, is actually fragmented at the neck of instabilities growing from its surface due to shearing stress. It is equivalent to individually inject drops of about 200 µm in diameter with a space of 0.9 mm between each of them. The typical injection frequency is therefore 33 kHz. When fragmented, the drops result in clouds composed of a dense head and a tail further downstream containing droplets and particles. The y-component of injection velocity is conserved during the whole fragmentation process because the y-distance between each cloud is roughly constant and the time for the liquid to reach the axis of the torch, i.e. radially travelling about 3 mm, is about 100 µs. The latter is evidently much higher than the characteristic time of fragmentation but also that of acceleration. Indeed, the x-distance between the heads of the first and third clouds is about 1 mm while it is 3 mm for the corresponding tails. Given the time between the first cloud and third cloud is 66µs, the x-velocity component of the head of the third cloud is 15 m.s^{-1} whereas that of its tail is 45 m.s^{-1}.

The fragmentation processes are inherently related to fluid instabilities and hence difficult to control because of plasma fluctuations in time (~10-250 µs) and of the radial gradients of plasma properties. The mechanical fragmentation can be delayed or even canceled out by changing the liquid properties (surface tension mainly) but also by handling smaller droplets leading to very low Weber number, favoring the smooth radial gradients with laminar jet and controlling the injection timing following the arc instabilities.

The dc pulsed torch presented in the previous section has been associated with a piezoelectric injection to perform a phased injection triggered by the torch itself according to a time delay τ depicted in Figure 3. Figure 5B displays the injection of precursor solution droplets (80 µm in diameter) in N_2 plasma jet. The fragmentation mechanism is completely different from that of Figure 5A because the Weber number is lower that unity owing the low plasma speed (70 m.s^{-1}). Moreover, the characteristic time of solvent vaporization is given by (37):

$$\tau_{vap} = \frac{\rho_L H_{vap}}{4 N_u a_\varphi} \left(\frac{d^2}{\bar{h}_0}\right) \left(1 - \left(\frac{d_s}{d_L}\right)^2\right) \tag{4}$$

where H_{vap}, d_s, N_u and a_φ are respectively the latent of solvent vaporization, the diameter of the solid phase after vaporization, the Nusselt number and the coefficient of heat potential (14). In a laminar flow, the acceleration time for the droplet is $\tau_{acc} = \rho_L d_L^2/18\eta$, where η is the dynamic viscosity of the plasma.

Considering the mean specific enthalpy given by Figure 2b, the vaporization time is about 100 µs while the acceleration time is higher than 2 ms. Note that the equation (4) is also related to the coefficient a_φ, namely the proportionality constant between the specific enthalpy and the heat potential of the plasma gas, so that it can be 2.5 times higher in the case of Ar-H_2 (75-25 vol%) than with pure N_2. Consequently, it can be assumed that thermal transfers occur during the slow acceleration phase leading to, as shown in Figure 5B1, a thermal fragmentation. The latter generate condensed material fragments treated further downstream by the plasma. Figures 5B2 and 5B3 depict the trajectories of such fragments during the exposure time which axial component velocities is between 30 and 55 m.s^{-1}. It is interesting to observe that close to the substrate some fragments follow the plasma streamlines as expected when evaluating the Stokes number of particles which is below unity. However, it has been shown that submicron-sized solid particles are trapped within the coatings that is why the liquid evaporation in Figure 5B1 results in the solution precipitation, probably also in in-flight molten particles and in the formation of crystallized γ-Al_2O_3 solid particles within the coating (37). Analogous phenomena are highlighted when spraying a ceramic ink of TiO_2 nanoparticles giving rise to micro-sized molten particles onto the substrate (51) suggesting an in-flight coalescence of nanoparticles.

Figure 5B also highlights significant amount of vapors that are pointed out by Figure 6. It depicts the molecular emission spectra of AlO ($B^2\Sigma^+ - X^2\Sigma^+$) between 430 and 550 nm for different distances from the nozzle exit (9, 18 and 30 mm where the coatings are deposited). It has to be underlined that the spectra are recorded when the arc voltage reaches its mean value (Figure 4). The spectrum obtained for the time-shift condition (at 30 mm) corresponds to a droplet emission by the printing head when the arc voltage is at its minimum value. Each spectrum integrates the radiative emission from all the height of sight (Y vertical direction, Y=0 being the torch axis). The progressive decomposition of the precursor is observed along with the formation of the AlO molecule which is supposed to form alumina ($2AlO_{(g)} + O \rightarrow Al_2O_{3(liq)}$). The emission profiles following the height of sight reveal inhomogeneities in the AlO species number distribution and a higher emission in the plasma fringes in contact with the oxygen of the surrounding air. The time-shifted spectrum has significant lower emission assuming a lower plasma temperature and stressing the influence of the synchronization of liquid injection on in-flight heat transfers.

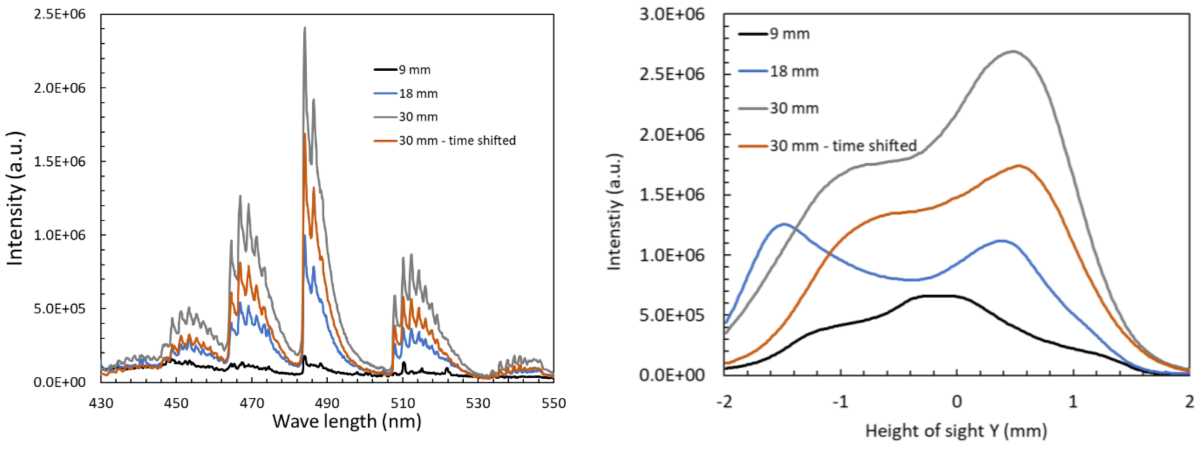

Figure 6. a) Emission spectra of AlO ($B^2\Sigma^+ - X^2\Sigma^+$) b) Emission profile following the height of sight for different distances from the nozzle exit. The acquisition of spectra is performed at the mean arc voltage for an exposure time of 60µs. The time-shifted condition corresponds to an arc voltage at its minimum value. The Y-direction is perpendicular to the torch axis referenced by zero.

The coating deposition resulting from the piezoelectric phased droplet injection lead mostly to very porous cauliflower shaped microstructures composed of nanometric grains that suggests the vapor condensation onto the substrate (37,51). This growth mechanism is profoundly different from that usually highlighted in SPS and SPPS at much higher liquid flow rates and relies on the stacking of micron-sized lamella on the substrate as explained in the next section.

4. Coatings growth

Many studies including numerous review papers report that typical SPS and SPPS coatings are formed from lamella resulting from fine melted particles conveyed by the plasma (11,52–56). For SPS, just after solvent evaporation, agglomeration and sintering of submicron particles are assumed (11). For SPPS, the solvent evaporation leads to consecutive complex transformations of the precursor solution, namely, precipitation, pyrolysis, sintering and melting (4). These transformation processes and their influences on coating features, especially its columnar structure and the porosity content, are dependent on solvent properties, material loads (%wt fraction of solid particles for SPS or molarity for SPPS), injection locations and modes (radial, axial), plasma torch properties, surface topography and shape of substrate. The coatings growth mechanisms are strongly influenced by the shadowing effect favoring a columnar growth (8,9). They are conceptualized by means of the Stokes (St) number of fine particles which encompasses all the thermal and dynamic history of particles and which is evaluated closed to the stagnation point during deposition. For very low St number, the speed component of particles parallel to the substrate ($v_{\parallel}$) is much higher than perpendicular one ($v_{\perp}$). Particles follow the deviated plasma streamlines and give rise to wider column and smaller inter-columnar voids. Dense coatings can be reached by increasing the plasma enthalpy and speed by favoring the increase of $v_{\perp}$ but also by improving the liquid fragmentation and evaporation (22,57).

In some of the applications such as photocatalysis, SPPS offers porous nano-structured films of higher specific surface area suitable for effective photocatalytic action. These materials form different nanostructures during SPPS process. Especially with ZnO, it tends to form nano-wires (NWs), nano-rods (NRs) or cauliflower like structures when subject to different plasma operating parameters. Studies on ZnO coatings formation using SPPS technique separately and in conjunction with different metal oxides have been reported by Yu et al. (58–62) as shown in Figure 7.

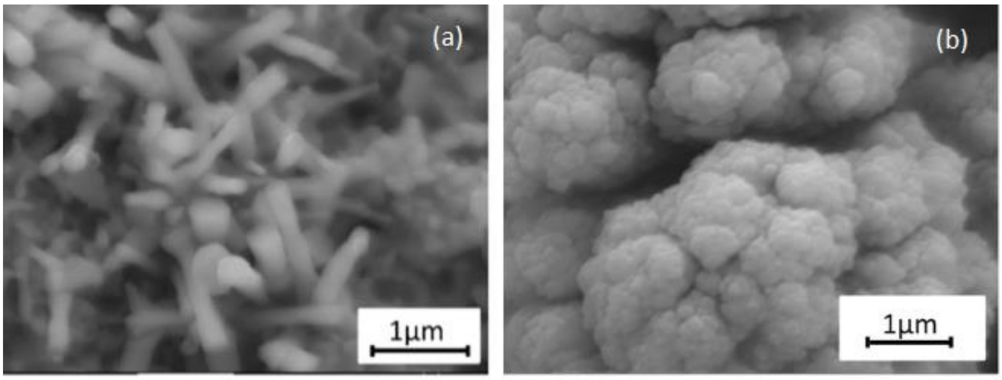

Figure 7. ZnO (a) nanorods (b) cauliflower like structure (62)
(Reproduced with kind permission of Elsevier)

An interesting observation on different morphologies of ZnO as a function of substrate distance from plasma jet, plasma composing species, substrate temperature and precursor injection mode (mixed or layered) has been reported. Study shows that the substrate distance from plasma is crucially playing role in deciding the morphology. Also, the molarity of the solution or the concentration of Zn in the precursor is also affecting the morphology.

Formation of different microstructures of the same material subjected to different operating regimes can be probed with the help of a nucleation and growth modelling tool. During a vapour phase synthesis of particles in thermal plasma, the cooling rate of plasma jet gas (typically between $10^4 – 10^6$ K/s) and initial monomer concentration which is dependent on concentration of the injected precursor, affect the supersaturation of nucleating species. More is the monomer concentration, supersaturation ratio mounts quickly at higher temperature as can be seen from Figure 8 (63). With decrease in monomer concentration (or precursor feeding rate), the species are nucleating at relatively lower temperature with higher supersaturation ratio as shown in Figure 8 where the supersaturation of yttria vapours is calculated for different initial mass flow rate and cooling rates. Another important factor is the cooling rate experienced by the vapours as they are passing the plasma jet down towards the substrate. The cooling rate is affected by the plasma gas velocity and spatial temperature fall (or gradient) at the plasma tail. Shaper is the temperature gradient or more is the plasma gas velocity, faster is the drop in the plasma temperature. This is arresting a further growth of the nucleated particles. This decides the final distribution of particle size. Faster is the quenching, particles will be ending up in a narrow size distribution.

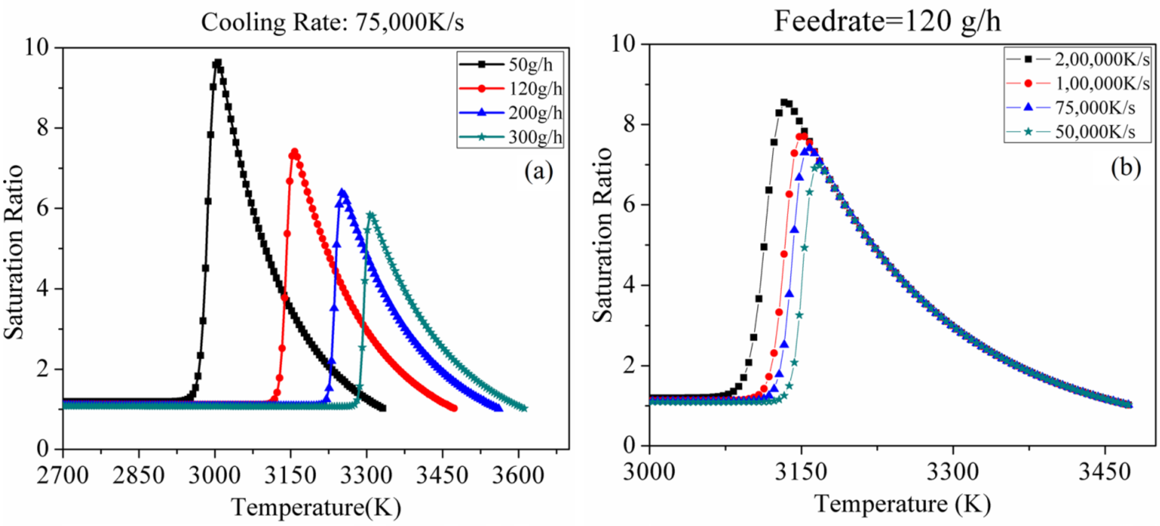

Figure 8. Supersaturation ratio for Y_2O_3 at (a) different initial concentration with fixed cooling rate and (b) different cooling with fixed monomer concentration (63)

(Reproduced with kind permission of IOP)

Thus, the parameters which affect the process of nucleation and growth can be listed as: degree of cooling of the saturated vapours, initial concentration of the vapours in the plasma, vapour pressure and surface tension of the nucleating species, and substrate temperature etc.

A rapid fall in the temperature stops the further growth of the particle while a constant heating with relatively low temperature near the substrate forces the particles to grow heterogeneously favouring the formation of nanostructures like NRs, NWs or a cauliflower like structure. In conclusion, the initial precursor concentration, effective heat flux by plasma at the substrate surface, governed by the plasma specific enthalpy and speed, the plasma cooling rate are deciding parameters for different nanostructure formation.

5. Conclusion

Plasma spraying of liquid feedstock has been studied for about two decades because of improved finely structured coatings properties resulting from the use of submicron particles, especially in the application fields of aeronautical, automotive and health. Many research studies have permitted to identify the relationships between the coating functionalities and the key operating parameters of the four main domains, i.e. 1) the plasma properties (linked to the plasma torch), 2) the thermo-physical properties of liquids containing particles or precursor solution, 3) the injection mode and 4) the deposition methodology.

However, the control of coating properties and the precise understanding of involved phenomena are still lacking because of, first, the intricate influences of the above mentioned four domains that requires each a close examination while considering their interdependence. Second, a multiscale approach of processes description must encompass transient phenomena (arc instabilities, heat and momentum transfers, liquid fragmentation and evaporation, particle transport with change of the phase, in-flight solid formation and coating growth) which considerably challenge in developing appropriate diagnostics and models. Third, the fine description of phenomena must give rise to the control of coating properties at macroscopic level.

To this end, the improvement of the plasma source acts as a leverage by controlling the arc instabilities with proactive strategies like the use of segmented plasma torches or alternatively applying a modulated DC arc current to strengthen in a controlled way the arc fluctuations. Moreover, the arc root attachment modes at the anode wall have to be considered in regards to the arc stability and the anode erosion due the possible co-existence of multiple arc roots. It is then expected that the flow regime of the resulting arc plasma jet affects the thermal decomposition of the liquid phase precursors, injected as suspensions or precursors solutions, depending on fragmentation processes. Especially for low Weber number, a thermal fragmentation has been shown to be strongly anisotropic sowing micron-sized material fragments in the plasma and generating strong material evaporation. In the particular case of aqueous suspension, during the solvent evaporation, the submicron particles trapped within a droplet tend to agglomerate due to the loss of electrostatic repulsion established by the ionized species of the water solvent. The coating growth of SPS and SPPS is being well understood from the velocity components of solid particles close to the substrate and their impact onto the substrate as fine lamella. Challenging efforts should be dedicated to develop diagnostics in the deposition region close to the substrate to not only establish a direct correlation between the particle impact velocity and the coating columnar features but also to elucidate the formation mechanisms of typical nanostructures like nanorods and nanowires obtained with SPPS.

References

1. E. Bouyer, F. Gitzhofer, and M. Boulos. Parametric study of suspension plasma sprayed hydroxyapatite. in ITSC 1996 (ed) CC Berndt (pub) ASM int Materials Park, OH, USA. 1996;683-91.
2. F. Gitzhofer, E. Bouyer and M.I. Boulos. Suspension plasm spray deposition. 5602921, 1997.
3. Karthikeyan J, Berndt CC, Tikkanen J, Reddy S, Herman H. Plasma spray synthesis of nanomaterial powders and deposits. Materials Science and Engineering: A. 1997;238(2):275-86.
4. Fauchais P, Etchart-Salas R, Delbos C, Tognonvi M, Rat V, Coudert JF, et al. Suspension and solution plasma spraying of finely structured layers: potential application to SOFCs. J Phys D: Appl Phys. 2007;40(8):2394-406.
5. Kassner H, Siegert R, Hathiramani D, Vassen R, Stoever D. Application of Suspension Plasma Spraying (SPS) for Manufacture of Ceramic Coatings. J Therm Spray Tech. 2008;17(1):115-23.
6. Jordan EH, Xie L, Gell M, Padture NP, Cetegen B, Ozturk A, et al. Superior thermal barrier coatings using solution precursor plasma spray. J Therm Spray Tech. 2004;13(1):57-65.
7. VanEvery K, Krane MJM, Trice RW, Wang H, Porter W, Besser M, et al. Column Formation in Suspension Plasma-Sprayed Coatings and Resultant Thermal Properties. J Therm Spray Tech. 2011;20(4):817-28.
8. Chidambaram Seshadri R, Dwivedi G, Viswanathan V, Sampath S. Characterizing Suspension Plasma Spray Coating Formation Dynamics through Curvature Measurements. J Therm Spray Tech. 2016;25(8):1666-83.
9. Bernard B, Bianchi L, Malié A, Joulia A, Rémy B. Columnar suspension plasma sprayed coating microstructural control for thermal barrier coating application. Journal of the European Ceramic Society. 2016;36(4):1081-9.
10. Jordan EH, Jiang C, Gell M. The Solution Precursor Plasma Spray (SPPS) Process: A Review with Energy Considerations. Journal of Thermal Spray Technology. 2015;24(7):1153-65.
11. Fazilleau J, Delbos C, Rat V, Coudert JF, Fauchais P, Pateyron B. Phenomena Involved in Suspension Plasma Spraying Part 1: Suspension Injection and Behavior. Plasma Chem Plasma Process. 2006;26(4):371-91.

12. Coudert JF, Chazelas C, Rigot D, Rat V. From transferred arc to plasma torches. High Temp Mat Proc. 2005;9(2):173-94.
13. Planche MP, Coudert JF, Fauchais P. Velocity Measurements for Arc Jets Produced by a DC Plasma Spray Torch. Plasma Chemistry and Plasma Processing. 1998;18(2):263-83.
14. Rat V, Coudert JF. A simplified analytical model for dc plasma spray torch: influence of gas properties and experimental conditions. J Phys D: Appl Phys. 2006;39(22):4799-807.
15. Zhukov MF, Zasypkin IM, éditeurs. Thermal plasma torches: design, characteristics, applications. Cambridge: Cambridge International Science Publ; 2007. 596 p.
16. Fauchais PL, Heberlein JVR, Boulos MI. Thermal Spray Fundamentals [Internet]. Boston, MA: Springer US; 2014. http://link.springer.com/10.1007/978-0-387-68991-3
17. Schein J, Richter M, Landes KD, Forster G, Zierhut J, Dzulko M. Tomographic Investigation of Plasma Jets Produced by Multielectrode Plasma Torches. J Therm Spray Tech. 2008;17(3):338-43.
18. Zhukovskii R, Chazelas C, Rat V, Vardelle A, Molz R. Predicted Anode Arc Attachment by LTE (Local Thermodynamic Equilibrium) and 2-T (Two-Temperature) Arc Models in a Cascaded-Anode DC Plasma Spray Torch. J Therm Spray Tech [Internet]. 9 sept 2021 https://link.springer.com/10.1007/s11666-021-01253-4
19. Ghorui S. Unique Aspects of Thermal Plasma Torches and Reactor Design for Process Applications. IEEE Trans Plasma Sci. 2021;49(2):578-96.
20. Zimmermann S, Schein J, Mauer G, Karl-Heinz R. Investigation and new physical behaviour of specila DC-Plasma generator Mettech Axial III. In: Proceedings of the International Thermal Spray Conference. Orlando, Florida, USA: F. Azarmi, K. Balani, T. Eden, T. Hussain, Y.-C. Lau, H. Li, K. Shinoda, F.-L. Toma, J. Veilleux; 2018. p. 818-24.
21. Spores R, Pfender E. Flow structure of a turbulent thermal plasma jet. Surface and Coatings Technology. 1989;37(3):251-70.
22. Dolmaire A, Hartikainen E, Goutier S, Béchade E, Vardelle M, Geffroy P-M, et al. Benefits of Hydrogen in a Segmented-Anode Plasma Torch in Suspension Plasma Spraying. J Therm Spray Tech. 2021;30(1-2):236-50.
23. Cao X, Li C, Chen L, Huang B. Experimental Study on the Design and Characteristics of a Laminar Plasma Torch With Medium Working Power and its Applications for Surface Hardening. IEEE Trans Plasma Sci. 2020;48(4):961-8.

24. Liu S-H, Zhang S-L, Li C-X, Li L, Huang J-H, Trelles JP, et al. Generation of Long Laminar Plasma Jets: Experimental and Numerical Analyses. Plasma Chem Plasma Process. 2019;39(2):377-94.
25. Caruyer C, Vincent S, Meillot E, Caltagirone J-P, Damiani D. Analysis of the unsteadiness of a plasma jet and the related turbulence. Surface and Coatings Technology. 2010;205(4):1165-70.
26. Solonenko OP, Nishiyama H, Smirnov AV, Takana H, Jang J. Visualization of arc and plasma flow patterns for advanced material processing. J Vis. 2015;18(1):1-15.
27. Pan W, Zhang W, Zhang W, Wu C. Generation of long, laminar plasma jets at atmospheric pressure and effects of flow turbulence. Plasma Chemistry and Plasma Processing. 2001;21(1):23-35.
28. Cao X, Li C, He R, Xu H, Chen L, Huang B. Study on the influences of the anode structures on the jet characteristics of a laminar plasma torch. Plasma Res Express. 2020;2(1):018001.
29. Liu S-H, Trelles JP, Murphy AB, Li L, Zhang S-L, Yang G-J, et al. Numerical simulation of the flow characteristics inside a novel plasma spray torch. J Phys D: Appl Phys. 2019;52(33):335203.
30. Krowka J, Rat V, Coudert JF. Investigation and control of dc arc jet instabilities to obtain a self-sustained pulsed laminar arc jet. J Phys D: Appl Phys. 2013;46(50):505206.
31. Mavier F, Zoubian F, Rat V. Electric arc in a plasma spray torch under modulated current. Journal of Physics D: Applied Physics. 2018;51(40):405201.
32. Heji Huang, Wenxia Pan, Chengkang Wu. Arc Root Motion in an Argon-Hydrogen DC Plasma Torch. IEEE Trans Plasma Sci. 2008;36(4):1050-1.
33. Dorier J-L, Gindrat M, Hollenstein C, Salito A, Loch M, Barbezat G. Time-resolved imaging of anodic arc root behavior during fluctuations of a DC plasma spraying torch. IEEE Trans Plasma Sci. 2001;29(3):494-501.
34. Yang G, Heberlein J. Anode attachment modes and their formation in a high intensity argon arc. Plasma Sources Sci Technol. 2007;16(3):529-42.
35. Wenxia Pan, Xian Meng, Teng Li, Xi Chen, Chengkang Wu. Comparative Observation of Ar, Ar-H $_2$ and Ar-N $_2$ DC Arc Plasma Jets and Their Arc Root Behaviour at Reduced Pressure. Plasma Sci Technol. 2007;9(2):152-7.
36. Wenxia Pan, Lewen Chen, Xian Meng X, Yong Zhang, Chengkang Wu. Sufficiently diffused attachment of nitrogen arc by gasdynamic action. Theoretical and Applied Mechanics Letters. 2016;6(6):293-6.

37. Mavier F, Zoubian F, Bienia M, Coudert JF, Lejeune M, Rat V, et al. Plasma spraying of solution precursor in pulsed mode: In-flight phenomena and coating deposition. Plasma Chemistry and Plasma Processing. 2018;38(4):657-82.
38. Duan Z, Heberlein J. Arc Instabilities in a Plasma Spray Torch. Journal of Thermal Spray Technology. 2002;11(1):44-51.
39. Shao K, Hu Y-H, Meng X, Huang H-J, Sun S-R, Wang H-X. Experimental Study on the Restrike Mode of a DC Arc Anode Attachment. Plasma Chem Plasma Process. 2021;41(5):1517-34.
40. Ghorui S, Tiwari N, Meher KC, Jan A, Bhat A, Sahasrabudhe SN. Direct probing of anode arc root dynamics and voltage instability in a dc non-transferred arc plasma jet. Plasma Sources Sci Technol. 2015;24(6):065003.
41. Qiang S, Yonghong L, Yancong H, Xinlei W, Peng L, Hui J. A novel experimental method of investigating anode-arc-root behaviors in a DC non-transferred arc plasma torch. Plasma Sources Sci Technol. 2020;29(2):025008.
42. Reis N, Derby B. Ink jet deposition of ceramic suspensions: Modelling and experiments of droplet formation. In S. C. Danforth, D. Dimos, et F. B. Prinz; 2000. p. 117-22.
43. Bienia M, Lejeune M, Chambon M, Baco-Carles V, Dossou-Yovo C, Noguera R, et al. Inkjet printing of ceramic colloidal suspensions: Filament growth and breakup. Chemical Engineering Science. 2016;149:1-13.
44. Derjaguin B, Landau L. Theory of the stability of strongly charged lyophobic sols and of the adhesion of strongly charged particles in solutions of electrolytes. Progress in Surface Science. 1993;43(1-4):30-59.
45. Liang Y, Hilal N, Langston P, Starov V. Interaction forces between colloidal particles in liquid: Theory and experiment. Advances in Colloid and Interface Science. 2007;134-135:151-66.
46. Jadidi M, Moghtadernejad S, Hanson J. Numerical Study of the Effects of Twin-Fluid Atomization on the Suspension Plasma Spraying Process. Fluids. 2020;5(4):224.
47. Jadidi M, Vardelle A, Dolatabadi A, Moreau C. Heat Transfer in Suspension Plasma Spraying. In: Handbook of Thermal Science and Engineering [Internet]. Cham: Springer International Publishing; 2018. p. 2923-66. http://link.springer.com/10.1007/978-3-319-26695-4_30
48. Meillot E, Vincent S, Caruyer C, Damiani D, Caltagirone JP. Modelling the interactions between a thermal plasma flow and a continuous liquid jet in a suspension spraying process. J Phys D: Appl Phys. 2013;46(22):224017.

49. Dalir E, Dolatabadi A, Mostaghimi J. Modeling of Suspension Plasma Spraying Process Including Arc Movement Inside the Torch. J Therm Spray Tech. 2019;28(6):1105-25.
50. Dalir E, Moreau C, Dolatabadi A. Three-Dimensional Modeling of Suspension Plasma Spraying with Arc Voltage Fluctuations. J Therm Spray Tech. 2018;27(8):1465-90.
51. Mavier F, Rat V, Bienia M, Lejeune M, Coudert J-F. Suspension and precursor solution plasma spraying by means of synchronous injection in a pulsed arc plasma. Surface and Coatings Technology. 2017;318:18-27.
52. Vaßen R, Kaßner H, Mauer G, Stöver D. Suspension Plasma Spraying: Process Characteristics and Applications. J Therm Spray Tech. 2010;19(1-2):219-25.
53. Killinger A, Gadow R, Mauer G, Guignard A, Vaßen R, Stöver D. Review of New Developments in Suspension and Solution Precursor Thermal Spray Processes. J Therm Spray Tech. 2011;20(4):677-95.
54. Unabia R, Candidato R, Pawłowski L. Current Progress in Solution Precursor Plasma Spraying of Cermets: A Review. Metals. 2018;8(6):420.
55. Fauchais P, Vardelle M, Goutier S, Vardelle A. Specific Measurements of In-Flight Droplet and Particle Behavior and Coating Microstructure in Suspension and Solution Plasma Spraying. J Therm Spray Tech. 2015;24(8):1498-505.
56. Dalir E, Dolatabadi A, Mostaghimi J. Modeling the effect of droplet shape and solid concentration on the suspension plasma spraying. International Journal of Heat and Mass Transfer. 2020;161:120317.
57. Chen D, Jordan EH, Gell M. The Solution Precursor Plasma Spray Coatings: Influence of Solvent Type. Plasma Chem Plasma Process. 2010;30(1):111-9.
58. Yu Z, Chouchene B, Liu M, Moussa H, Schneider R, Moliere M, et al. Influence of laminated architectures of heterostructured CeO2-ZnO and Fe2O3-ZnO films on photodegradation performances. Surface and Coatings Technology. 2020;403:126367.
59. Yu Z, Moussa H, Liu M, Schneider R, Wang W, Moliere M, et al. Development of photocatalytically active heterostructured MnO/ZnO and CuO/ZnO films via solution precursor plasma spray process. Surface and Coatings Technology. 2019;371:107-16.
60. Yu Z, Moussa H, Ma Y, Liu M, Chouchene B, Schneider R, et al. Oxygen-defective ZnO films with various nanostructures prepared via a rapid one-step process and corresponding photocatalytic degradation applications. Journal of Colloid and Interface Science. 2019;534:637-48.

61. Yu Z, Moussa H, Liu M, Chouchene B, Schneider R, Wang W, et al. Tunable morphologies of ZnO films via the solution precursor plasma spray process for improved photocatalytic degradation performance. Applied Surface Science. 2018;455:970-9.
62. Yu Z, Moussa H, Liu M, Schneider R, Moliere M, Liao H. Solution precursor plasma spray process as an alternative rapid one-step route for the development of hierarchical ZnO films for improved photocatalytic degradation. Ceramics International. 2018;44(2):2085-92.
63. Dhamale GD, Tak AK, Mathe VL, Ghorui S. Nucleation and growth of Y2O3 nanoparticles in a RF-ICTP reactor: A discrete sectional study based on CFD simulation supported with experiments. Journal of Physics D: Applied Physics. 2018;51(25):aac3f1.